1

Introduction

This chapter introduces the background information and basic concepts of optical remote sensing. *Optical remote sensing* refers to wavelengths ranging from the visible spectrum to the thermal infrared (IR) spectrum (0.4–14 μm). This chapter basically consists of two parts. The first part (Sections 1.1 and 1.2) discuss various radiometric variables that will be extensively used in the book, and the second part (Section 1.3) briefly describes the major components of a remote sensing modeling system that links remotely sensed data with land surface variables, which serves as the pointers to various chapters and sections in the rest of the book. For some topics that are not discussed in detail later, more details will be presented in this chapter.

Section 1.1 classifies all quantitative models for retrieving land surface variables from optical remotely sensed data into three major categories: statistical, physical, and hybrid. Their major characteristics are briefly discussed. Section 1.2 defines some basic physical concepts and illustrates the conversion from digital numbers to a series of physical variables that will be discussed in the following chapters in more detail. Section 1.3 discusses the major components of a remote sensing modeling system on which physical models are based. The concepts of forward modeling and inversion methods are also illustrated.

1.1 QUANTITATIVE MODELS IN OPTICAL REMOTE SENSING

All models in optical remote sensing are traditionally grouped into two major categories: statistical and physical. *Statistical models* are based on correlation relationships of land surface variables and remotely sensed data. They are easy to develop and effective for summarizing local data; however, the

---

Quantitative Remote Sensing of Land Surfaces. By Shunlin Liang
ISBN 0-471-28166-2

developed models are usually site-specific. They also cannot account for cause–effect relationships.

On the other hand, physically based models follow the physical laws of the remote sensing system. They also establish cause and effect relationships. If the initial models do not perform well, we know where to improve by incorporating the latest knowledge and information. However, there is a long curve to develop and learn these physical models. Any models represent the abstract of the reality; thus a realistic model could potentially be very complex with a large number of variables.

There is a new trend in remote sensing to develop hybrid models that combine both statistical and physical models, that may take advantage of the unique features of each and overcome their shortcomings.

All three categories of quantitative models for estimating land surface variables will be presented systematically in Chapter 8 and also individually in several other chapters. All quantitative models in remote sensing utilize five signatures: spectral, spatial, temporal, angular, and polarization. Because of the scope of the book, we will not present any models based on polarization signatures.

Land surfaces can be characterized by *continuous variables* (e.g., leaf area index, albedo) and *categorical variables* (e.g., land cover) through various quantitative models. Because of the scope, we will address only continuous variables; thus, we have excluded a large group of image classification algorithms and applications (e.g., land cover and use and change mapping) out of this book.

1.2 BASIC CONCEPTS

1.2.1 Digital Numbers

Early statistical models in remote sensing often employed *digital numbers* (DNs) to estimate surface characteristic variables directly. DNs are what we get after purchasing data from the data providers. But DNs are the scaled integers from *quantization*, which is not a physical quantity. Although it might be desirable to use nonlinear quantization for low-reflectance cases such as oceanography, most quantization systems in remote sensing are linear, typically 6–12 bits. The DN can be any integer in the range

$$\mathrm{DN} \in [1, 2^{Q}] \tag{1.1}$$

where Q is an integer representing the bits. For example, an 8-bit ($Q = 8$ and $2^8 = 256$) linear quantization system equally divides the dynamic range of response of the sensor into 255 steps, from 1 to 256. The same response of the sensor will produce totally different DNs if a 10- or 12-bit quantization system is used. It is obvious that a larger Q leads to a higher radiometric precision. Table 1.1 shows the quantization levels for several common satel-

TABLE 1.1 Quantization Levels of Some Common Sensor Systems for Land Applications

Sensor	TM	SPOT	AVHRR	IKONOS	MODIS/MERIS
Q	8	8	10	11	12

lite sensor systems, the thematic mapper (TM) in the U.S. Landsat system, the French SPOT (Systeme pour l'Observation de la Terre) satellite system, the advanced very high-resolution radiometer (AVHRR), the private IKONOS satellite, moderate-resolution imaging spectroradiometer (MODIS), and medium-resolution imaging spectrometer (MERIS).

1.2.2 Radiance

We now realize that DNs should be converted to physical quantities for estimating land surface variables such as *radiance* (sometimes called *intensity*), measured in the energy per area per solid angle. The solid angle is explained in Section 1.2.3. Spectral (monochromatic) radiance represents the energy per area per solid angle per unit wavelength. A typical unit could be W cm^{-2} Sr^{-1} μm^{-1}, where sr (steradian) is the unit for measuring solid angles, and μm (micrometer) measures wavelength. Note that different units may be used in the literature and it is important to know their conversions. In particular, wavelength (λ: μm) in thermal infrared (IR) remote sensing is customarily specified by *wavenumber* ν, which is the reciprocal of the wavelength ($1/\lambda$). Traditionally, wavenumber is expressed in inverse centimeters, which is numerically equivalent to $10^4/\lambda$, where λ is in μm (1 cm = 10^4 μm). For example, the wavelength at 10 μm has a wavenumber of 1000 cm^{-1}. To convert radiance in (W cm^{-2} sr^{-1})/cm^{-1} to (W cm^{-2} sr^{-1})/μm, one must multiply by $\nu^2/10^4$.

Normally, DNs are linearly related to radiance, and most remote sensing data providers produce the conversion coefficients for the users. Sensors receive radiance at the range of wavelengths (waveband), but these conversion coefficients are typically for generating spectral radiance to avoid the difference of waveband widths. These coefficients are usually included in the image data header file (or metadata). The procedure that determines these conversion coefficients is called *sensor calibration*. It is an important procedure in remote sensing since many sensors deteriorate in space after the satellite launch and the preflight conversion coefficients seldom remain valid. A detailed description of sensor calibration will be discussed in Chapter 5.

1.2.3 Solid Angle

The directional dependence of radiance is taken into account by employing the *solid angle* (Ω), which is an extension of two-dimensional angle measure-

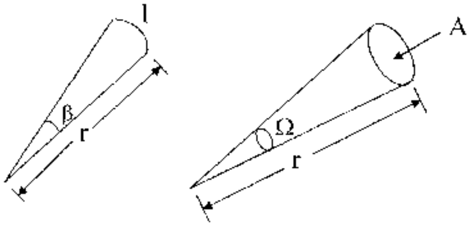

Figure 1.1 Planar angle (β) and solid angle (Ω).

ment. Understanding the angular dependence is very important since most sensors are targeting the Earth surface in a specific direction. As illustrated in Fig. 1.1, the angle β between two radii of a circle of radius r is

$$\beta = \frac{l}{r} \quad (\text{rad}) \tag{1.2}$$

The arc length of the full circle is $2\pi r$, so the angular measure of the full circle is 2π rad. The solid angle Ω is defined as the ratio of the area A of a spherical surface intercepted by the cone to the square of the radius

$$\Omega = \frac{A}{r^2} \quad (\text{sr}) \tag{1.3}$$

For a sphere whose surface area is $4\pi r^2$, its solid angle is 4π sr (steradians). Thus, the solid angle of the upper or lower hemisphere is 2π sr.

A solid angle is often represented by the zenith and azimuth angles in polar coordinates. If θ represents the zenith angle (the angle measured from the vertical or from the horizontal to a surface), ϕ represents the azimuth angle (Fig. 1.2), then a differential element of solid angle is mathematically given by

$$d\Omega = \frac{dA}{r^2} = \frac{(r\,d\theta)(r \sin\theta\, d\phi)}{r^2} = \sin\,\theta\, d\theta d\phi = d\mu d\phi \tag{1.4}$$

where $\mu = \cos\theta$. Note that the zenith angle θ ranges from 0 to 180°. In the literature, the range of 0–90° (i.e., $0 \le \mu \le 1$) usually represents the upwelling hemisphere and 90–180° (i.e., $-1 \le \mu \le 0$) the downward hemisphere, which will be used throughout this book. But this is arbitrarily defined, we can also find the exactly opposite definition in the literature. The azimuth angle ϕ ranges from 0 to 360°, that is, $0 \le \phi \le 2\pi$.

It is worth pointing out that the viewing zenith angle is not equivalent to the sensor scan angle that has been frequently used in the remote sensing literature. The difference can be observed in Fig. 1.3. If Earth is assumed to be a sphere, the relationship between the two angles can be easily expressed

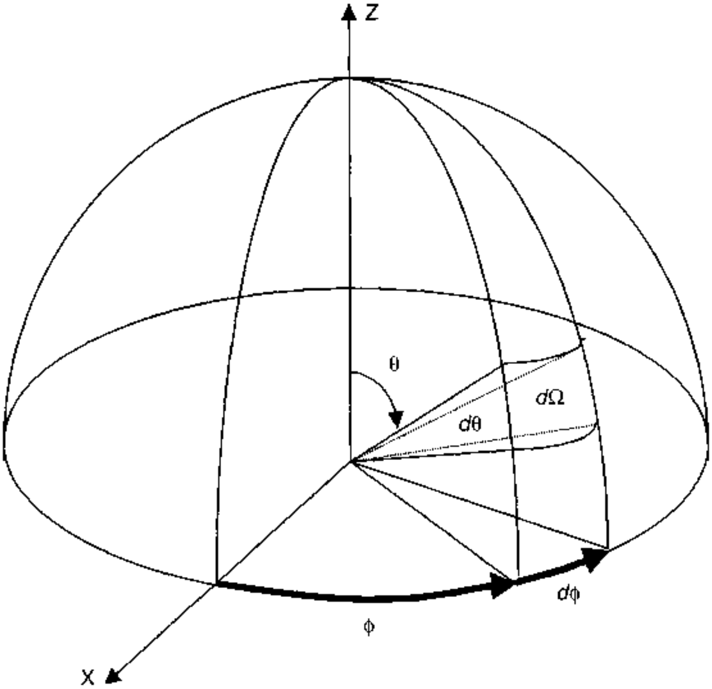

Figure 1.2 Illustration of the zenith angle (θ), azimuth angle (φ), and solid angle (Ω).

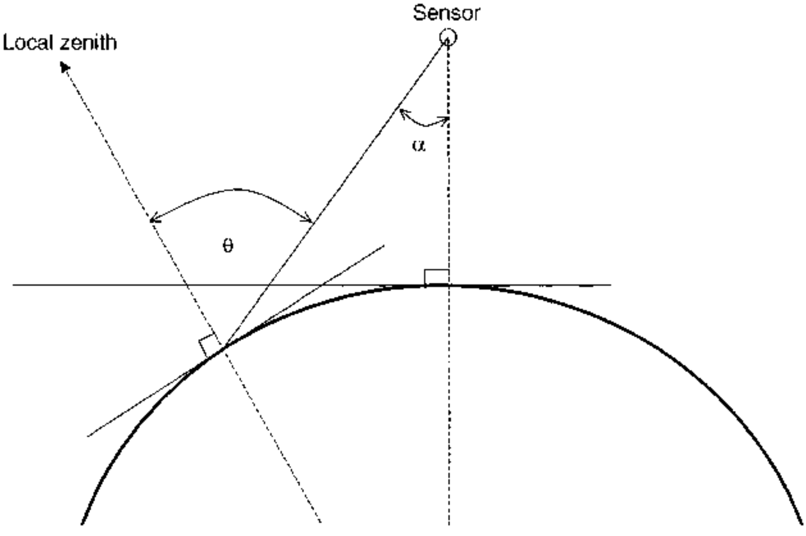

Figure 1.3 Relationship between the sensor scanning angle (α) and the viewing zenith angle (θ).

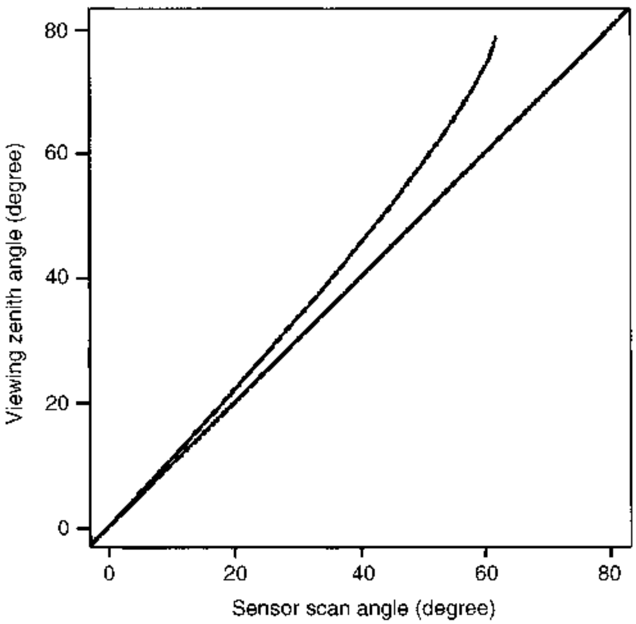

Figure 1.4 Numerical comparison of the local viewing zenith angle and the sensor scan angle.

as

$$\sin\theta = \frac{R_0 + h}{R_0}\sin\alpha \tag{1.5}$$

where the Earth radius is $R_0 = 6378$ km and h is the orbital height of the satellite above Earth. The typical height of the remote sensing satellites varies from 600 to 900 km (e.g., h = 705 km for Landsat-4 and -5, h = 832 for the first three SPOT (Systeme pour l'Observation de la Terre) satellites, h = 681 km for IKONOS, h = 705 km for Aqua). For h = 700 km, the relationship between the local viewing zenith angle and the sensor scanning angle is shown in Fig. 1.4. It is clear that the viewing zenith angle θ at a specific location of the Earth surface is always larger than the sensor's scan angle α. The larger the sensor scan angle, the larger their difference.

1.2.4 Irradiance

By definition, *irradiance* (E) is the integration of radiance (L) over the entire solid angle of a hemisphere consisting of the zenith angle θ and the azimuth angle ϕ:

$$E = \int_0^{2\pi}\int_0^{\pi/2} L(\theta,\phi)\cos\theta\sin\theta\, d\theta d\phi = \int_0^{2\pi}\int_0^{1} L(\mu,\phi)\mu\, d\mu d\phi \tag{1.6}$$

If radiance is independent of the direction (isotropic), Eq. (1.6) becomes $E = \pi L$. Note that irradiance is often called *flux density* or simply *flux* in the remote sensing literature.

1.2.5 Bidirectional Reflectances and Albedos

Upwelling radiance received by the Earth-viewing sensors depends on the incoming solar radiation. To normalize the variation of the incoming solar radiation, the top-of-atmosphere (TOA) radiance $I(\theta_v, \phi_v)$ converted from DN at the specific viewing direction (θ_v, ϕ_v) is often further converted into reflectance

$$R(\theta_i, \phi_i\, \theta_v, \phi_v) = \frac{\pi I(\theta_i, \phi_i, \theta_v, \phi_v)}{\cos\theta_i E_0} \tag{1.7}$$

where θ_i is the solar zenith angle and E_0 is the incoming TOA irradiance. It is not difficult to understand that reflectance obviously depends on both the solar incoming direction and the sensor viewing direction, which is usually denoted as *bidirectional reflectance factor*. The same concept is applied to land surface (Martonchik et al. 2000).

A complete description of the directional reflectance properties of a surface is provided by the *spectral bidirectional reflectance distribution function* (BRDF) $f(\theta_i, \phi_i\, \theta_v, \phi_v)$, which is defined as the ratio of the reflected spectral radiance from the surface in the direction θ_v, ϕ_v to the directional spectral irradiance on the surface in the direction θ_i, ϕ_i:

$$f(\theta_i, \phi_i, \theta_v, \phi_v) = \frac{dL(\theta_i, \phi_i\, \theta_v, \phi_v)}{dE(\theta_i, \phi_i)} \tag{1.8}$$

and has the units of reciprocal steradians. This concept has been extensively used in multiangle remote sensing, but in practice people tend to use the dimensionless *bidirectional reflectance factor* (BRF) EMBED $R(\theta_i, \phi_i, \theta_v, \phi_v)$, which is numerically equivalent to BRDF multiplied by π:

$$R(\theta_i, \phi_i, \theta_v, \phi_v) = \pi f(\theta_i, \phi_i, \theta_v, \phi_v) \tag{1.9}$$

Different statistical BRDF/BRF models are discussed in Section 2.2. Chapters 2–5 are devoted to introducing various physically based methods for calculating land surface BRDF/BRF. The in-depth reviews on this subject are available in a special issue of *Remote Sensing Reviews* (Liang and Strahler 2000).

For studies of surface shortwave energy balance (see Chapter 9) and other applications, we need surface *directional hemispherical reflectance* (DHR), which can be integrated from BRF over all reflected directions:

$$r(-\mu_i, \phi_i) = \frac{1}{\pi}\int_0^{2\pi}\int_0^1 R(\mu_i, \phi_i, \mu, \phi)\,\mu\, d\mu\, d\phi \tag{1.10}$$

DHR is often called *local* or *planar albedo*, but is called *black-sky albedo* in the MODIS products of the NASA Earth Observing System (EOS) program. *Bihemispherical reflectance* (BHR) is a further integration of DHR over all illumination directions

$$r_0 = 2\int_0^1 r(-\mu_i, \phi_i)\,\mu_i\, d\mu_i \tag{1.11}$$

which is also called *global* or *spherical albedo*, or *bright-sky albedo* in the MODIS products.

In the thermal IR spectrum, emissivity (ε) is much more often used than reflectance. $\varepsilon = 1 - r_0$ according to the Kirchhoff's law. More details are available in Chapter 10. Note that all these variables are the function of wavelength.

1.2.6 Extraterrestrial Solar Irradiance

Incoming TOA irradiance depends on the astronomical distance between the Sun and Earth (D). Given the solar irradiance $\overline{E}_0$ at the average Earth–Sun distance ($D = 1$), a simple expression can be used to approximate the solar irradiance on any day

$$E_0 = \frac{\overline{E}_0}{D^2} = \overline{E}_0\left[1 + 0.033\cos\left(\frac{2\pi d_n}{365}\right)\right] \tag{1.12}$$

where d_n is the day number of the year, ranging from 1 on January 1 to 365 on December 31; February is always assumed to have 28 days. A more accurate formula is

$$E_0 = \overline{E}_0[1.00011 + 0.034221\cos\chi + 0.00128\sin\chi + 0.000719\cos 2\chi + 0.000077\sin 2\chi] \tag{1.13}$$

where $\chi = 2\pi(d_n - 1)/365$. For most applications, Eqs. (1.12) and (1.13) will not make any significant difference.

There have been many efforts to compile the solar irradiance curves (Gao and Green 1995) with variable accuracies. The total irradiance integrated over all wavelengths is called the *solar constant*:

$$S_0 = \int_0^\infty \overline{E}_0(\lambda)\, d\lambda \tag{1.14}$$

The results of modern solar constant monitoring during the 1980s reveal that the average S_0 is around 1369 W/m^2 with an uncertainty of ±0.25% (Hartmann et al. 1999). It also has solar cycle variations. The new generation of sensors will provide more accurate observations.

There are four data sets available in MODTRAN4 compiled from different sources. MODTRAN is an atmospheric radiative transfer software package that has been widely used in various remote sensing applications, and more details on this package will be provided in this book from time to time. They are included in the CD-ROM (newkur.dat, chkur.dat, cebchkur.dat, and thkur.dat). The corresponding solar constants are 1362.12, 1359.75, 1368.00, and 1376.23 W/m^2. Figure 1.5a shows the spectral solar irradiance curve (W m^{-2} μm^{-1}) of thkur.dat from 0.2–3.5 μm, Fig. 1.5b–Fig. 1.5d show the difference between thkur.dat and three other datasets in the same unit from 0.2 to 1.0 μm. It is surprising to see that the differences are so significant, particularly over the visible spectrum.

We need to be very careful to select the right data source of the TOA solar irradiance when we analyze hyperspectral data, although this may not be a serious problem when we work with the multispectral remotely sensed data. For different sensors whose spectral response functions (see Section 1.3.5.1) are known, we can easily calculate $\overline{E}_0$ for each waveband by integrating TOA spectral solar irradiance with the sensor spectral response functions. For ease of reference, $\overline{E}_0$ of the six reflective bands of Landsat-4/5 thematic mapper and Landsat-7 enhanced thematic mapper plus (ETM +) and the two reflective bands of NOAA advanced very high-resolution radiometer (AVHRR) are listed in Tables 1.2 and 1.3. In fact, many sensor spectral response functions and these four TOA spectral irradiance datasets displayed in Fig. 1.5 are provided in the accompanying CD-ROM, and readers can easily generate similar numbers. Do not be surprised if you see different numbers for TM or ETM + in the literature since different TOA spectral solar irradiance datasets may be used.

TABLE 1.2 TOA Solar Irradiance of Landsat TM / ETM + Reflective Bands (W m^{-2} μm^{-1})

Bands	1	2	3	4	5	7	Pan[a]
ETM +	1970	1843	1555	1047	227.1	80.53	1368
TM	1954	1826	1558	1047	217.2	80.29	N/A

[a] Panchromatic band.

TABLE 1.3 TOA Solar Irradiance (W m^{-2} μm^{-1}) of NOAA AVHRR Band 1 (0.58 0.68 μm) and Band 2 (0.72–1.1 μm)

Bands	NOAA7	NOAA9	NOAA11	NOAA12	NOAA14	NOAA16
1	1643.5	1635	1629.2	1613.7	1628.1	1644
2	1051.8	1053.6	1052.8	1049.8	1029.8	1034

Source: Data derived from Neckel and Labs (1984).

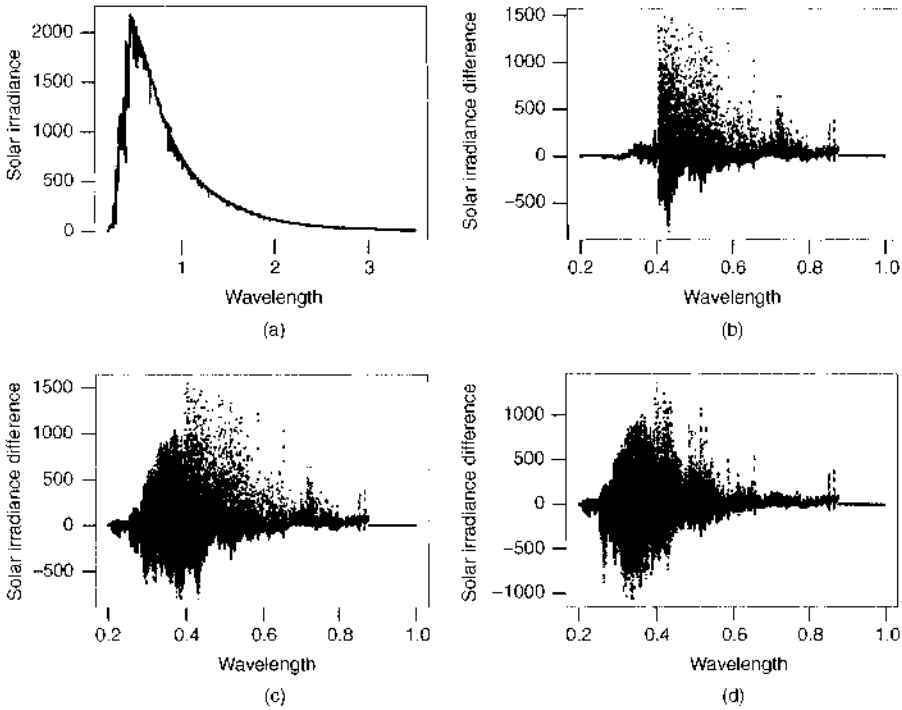

(a) (b)

(c) (d)

Figure 1.5 Solar extraterrestrial irradiance data sets included in MODTRAN4: (a) irradiance spectra data of thkur.dat; irradiance difference spectra are shown between (thkur.dat) and (cebchkur) (b), between (thkur.dat) and (chkur) (c), and between (thkur.dat) and (newkur) (d). The unit is W m^{-2} μm^{-1}.

1.3 REMOTE SENSING MODELING SYSTEM

An optical remote sensing system can be physically modeled with several subsystems: scene generation, scene radiation modeling, atmospheric radiative transfer modeling, navigation modeling, and mapping and binning. *A forward modeling scheme* predicts what remotely sensed data will be under a set of environmental and sensing conditions. *A physically based inversion scheme* determines various land surface geophysical and biophysical variables from remotely sensed data. Both schemes rely on a good physical understand-

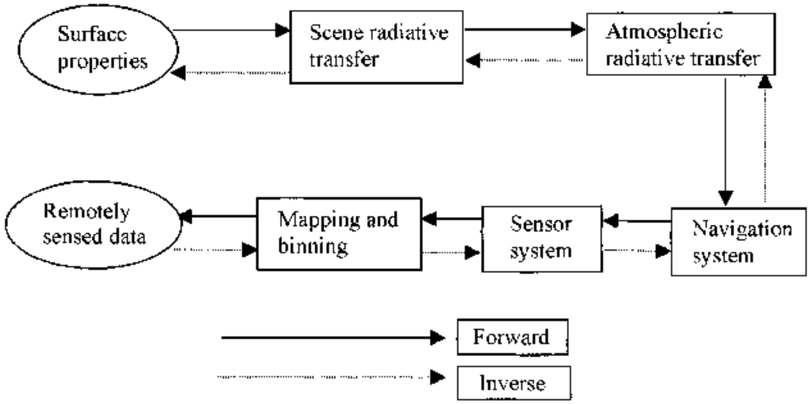

Figure 1.6 Illustration of a remote sensing modeling system (both forward and inversion schemes).

ing of different components in a remote sensing system (Fig. 1.6). Each individual component is briefly outlined below, and most of the components are discussed in more detail in later chapters. For further reading, readers are referred to some related textbooks for some of the components (e.g., Schott 1997, Schowengerdt 1997, Milman 1999)

1.3.1 Scene Generation

A scene generation model quantifies the relationships among the type, number, and spatial distribution of objects and the background in the scene of the land surface. It is a quantitative description of our understanding of the landscape. Strahler et al. (1986) identify two different scene models in remote sensing: H- and L-resolution (high- and low-resolution) models. The H-resolution models are applicable where the elements of the scene are larger than the pixel size; with the L-resolution model, the converse is true. L-resolution models can be regarded as a type of (continuous) mixture model where the proportions are functions of the sizes and shapes of the elements in the scene model and their relative densities within the pixel. H-resolution models are highly related to computer graphics. These techniques are relatively mature now, and motion pictures have been generated using similar techniques without any human actors. Many such algorithms are based on these two mathematical theories: fractals and L system.

Fractals are complex, detailed geometric patterns found throughout the natural world. They can be created using mathematical formulas and are infinite in their ability to be viewed in ever increasing detail. They are recursively defined and small sections of them are similar to large ones. One way to think of fractals for a function $f(x)$ is to consider x, $f(x)$, $f(f(x))$,

$f(f(f(x)))$, $f(f(f(f(x))))$, and so on. More details are available in the literature (e.g., Mandelbrot 1983, Fisher 1995).

Lindenmayer systems, or L systems for short, are a particular type of symbolic dynamical system with the added feature of a geometric interpretation of the evolution of the system. An L system is a formal grammar for generating strings. By recursively applying the rules of the L systems to an initial string, one can create a string with fractal structure. Interpreting this string as a set of graphical commands allows the fractal to be displayed. L systems are very useful for generating realistic plant structures (Prusinkiewicz and Lindenmayer 1990). L systems have been used for generating landscapes in computer simulation models (e.g., Monte Carlo ray tracing and radiosity), discussed in Sections 3.5.1 and 3.5.2.

Suppose that we want to generate a H-resolution forest scene. The first thing we need to know is the spatial distribution of the trees: regular or random. For regularly distributed canopies, we need to specify the row intervals. If they are randomly distributed, we need to specify the spatial distribution function (e.g., Poisson) and its characteristic parameters. We also need to specify the geometric parameters of the tree, such as the densities and dimensions of the leaves, trunk, and branches, and their space and inclination angles. Sometimes, we also need to specify the cluster density of the leaves and the locations of their central points. These parameters can be measured in the field. Some examples are given in Section 3.2.3.

In generating an L-resolution scene, it is not necessary to specify the shape and size of the individual elements since they cannot be distinguished within a pixel. There are two common numerical generation techniques. The first is based on the geographic information system (GIS) concept. The spatial distributions of different elements are expressed by using different data layers in a GIS environment. Overlapping these layers is one of the basic functions in any GIS software program that can generate an L-resolution scene. The second is based on stochastic field theory. The brightness of the scene is described by a random function. The common stochastic field functions used for generating remote sensing imagery include Gibbs random field and Markov random field. A discrete Gibbs random field is specified by a probability mass function of the image as follows:

$$P(x) = \frac{1}{Z} e^{[H(x)/T]} \tag{1.15}$$

where Z is the normalization factor, $H(x)$ is an energy function, and T represents temperature, $T = \Sigma H(x)$, over all G^n images; **G** is the number of pixel value levels, and the image is of size $\sqrt{n} \times \sqrt{n}$. Except in very special circumstances, it is not feasible to compute **T**. A relaxation-type algorithm described in the literature (e.g., Cross and Jain 1983, Dubes and Jain 1989) simulates a Markov chain through an iterative procedure that readjusts the gray levels at pixel locations during each iteration. This algorithm sequentially initializes the value of each pixel using a uniform distribution. Then a single pixel location is selected at random, and using the conditional distribution that describes the Markov chain, the new pixel value at that location is selected, dependent only on the pixel values of the pixels in its local neighborhood. The sequential algorithm terminates after a given number of iterations.

The Gaussian–Markovian random field (GMRF) models assume that pixel values have joint Gaussian distributions and correlations controlled by a number of parameters representing the statistical dependence of a pixel value on the pixel values in a symmetric neighborhood. There are two basic schemes for generating a GMRF image model: direct or iterative. More details can be found in the literature (e.g., Chellappa 1985, Jeng et al. 1993).

In geostatistics, a conditional simulation is an effective technique to generate the random field. Sequential Gaussian simulations, Gaussian simulations, nonparametric simulation techniques such as sequential indicator simulations, and probability field simulations are becoming more and more popular. Some of these algorithms are available in the public domain software packages, such as GSLIB (Deutsch and Journel 1992). The interested reader is referred to the textbooks on this subject (e.g., Journel and Huijbregts 1978, Isaaks and Srivastava 1989, Cressie, 1993).

1.3.2 Scene Radiation Modeling

There are roughly three types of models that characterize the radiation field of the scene and are mostly used in optical remote sensing: geometric optical models, turbid-medium radiative transfer models, and computer simulation models. In *geometric optical models*, canopy or soil is assumed to consist of geometric protrusions with prescribed shapes (e.g., cylinder, sphere, cones, ellipsoid, spheroid), dimensions, and optical properties that are distributed on a background surface in a defined manner (regularly or randomly distributed). The total pixel value is the weighted average of sunlit and shadowed components. The turbid-medium radiative transfer models treat surface elements (leaf or soil particle) as small absorbing and scattering particles with given optical properties, distributed randomly in the scene and oriented in given directions. The further development of geometric optical models has incorporated radiative transfer theory in calculating the individual sunlit/shadow components; the resulting models are often called *hybrid models*. In computer simulation models, the arrangement and orientation of scene elements are simulated on a computer and the radiation properties are determined on the basis of *radiosity* equations and/or *Monte Carlo ray tracing* methods. The details on these modeling methods for vegetation canopies will be given in Chapter 3 and for soil and snow in Chapter 4.

1.3.3 Atmospheric Radiative Transfer Modeling

The Earth's Atmosphere affects remote sensing imagery significantly. The atmospheric gases, aerosols, and clouds scatter and absorb the incoming solar radiation and the reflected and/or emitted radiation from the surface. As a result, it greatly modulates the spectral dependence and spatial distribution of the surface radiation. Therefore, understanding the atmospheric radiative transfer and correcting atmospheric effects from remotely sensed imagery are very critical for land surface characterization. These two topics are discussed in Chapters 2, 6, and 10 in detail.

1.3.4 Navigation Modeling

For a spaceborne remote sensing system, we must be able to calculate the position of the satellite in space, to track it from Earth and to know where the instruments are pointing. Despite their importance, positioning in space, tracking, and navigation are more or less the scientific and technical issues that engineers are mainly concerned with. Within the scope of this book, we will not provide with any more details on this subject. The interested reader is referred to other publications (e.g., Emery et al. 1989).

1.3.5 Sensor Modeling

The upwelling TOA radiance is recorded and modulated by a sensor. Sensor models characterize the process converting the spectral radiance of the land surface–atmosphere system into digital numbers that users obtain when purchasing from the data distribution centers. Figure 1.7 shows the block diagram of the sensor model. Sensor spectral response functions are integrated with scene spectral radiance to generate the band values, and spatial response functions define the pixel values with a discrete convolution of separable linespread functions in the two spatial dimensions. Noise can be modeled explicitly before the signals are converted to digital numbers by scaling each band. Because of their importance, we will focus on the sensor spectral response functions and spatial responses below.

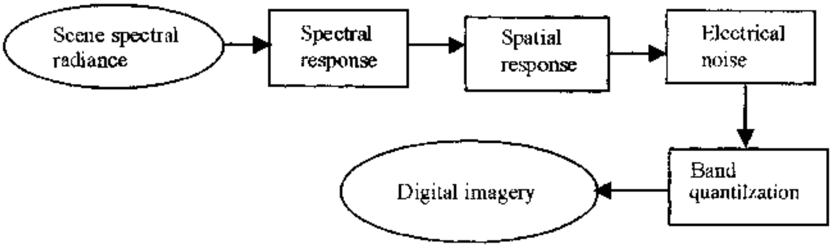

Figure 1.7 Flowchart of a sensor modeling system.

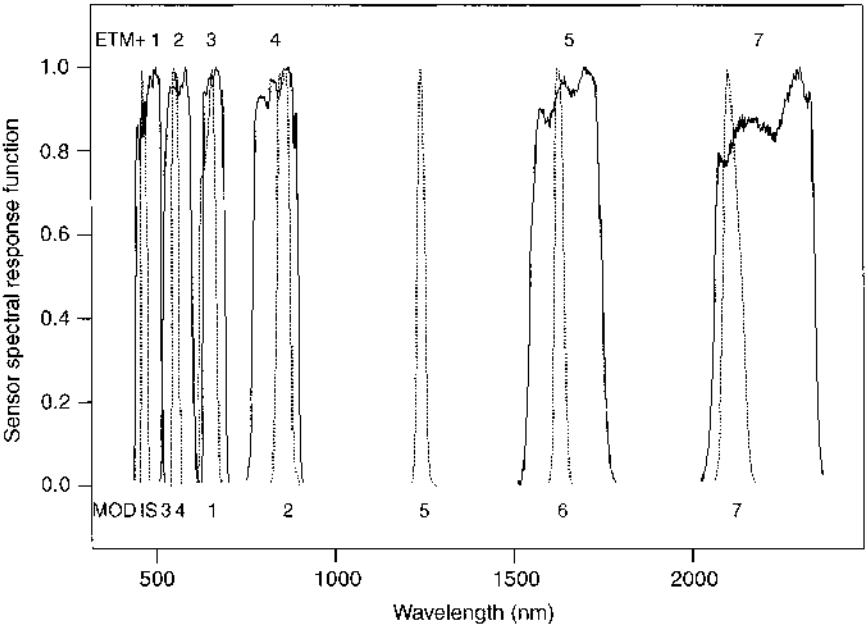

Figure 1.8 ETM + and MODIS visible and near-IR sensor spectral response functions. The solid lines correspond to ETM + and the dashed lines, to MODIS.

1.3.5.1 Spectral Response

Letting $L_{\lambda,\ \mathrm{sensor}}$ be the spectral radiance of the atmosphere-land surface scene reaching the sensor detectors, the resulting array, after the spectral response function $f(\lambda)$ is applied, is computed as follows:

$$L_b(x, y) = \frac{\int_{\lambda_{\min}}^{\lambda_{\max}} L_{\lambda,\mathrm{sensor}}(x, y) f(\lambda)\, d\lambda}{\int_{\lambda_{\min}}^{\lambda_{\max}} f(\lambda)\, d\lambda} \tag{1.16}$$

where x, y are pixel locations. Few radiative transfer solvers incorporate sensor spectral response functions in their software packages; users can easily calculate spectral radiance using Eq. (1.15). The sensor spectral response functions of the first few bands of ETM + and MODIS for land applications are shown in Fig. 1.8. The reader can make such a figure for many sensors whose spectral response functions are included in the CD-ROM accompanying this book.

Note that L_b is the effective (average) spectral radiance of a specific band. The band integrated radiance equals L_b multiplied by the effective *bandwidth*. Bandwidths of spectral responses are usually expressed as the full

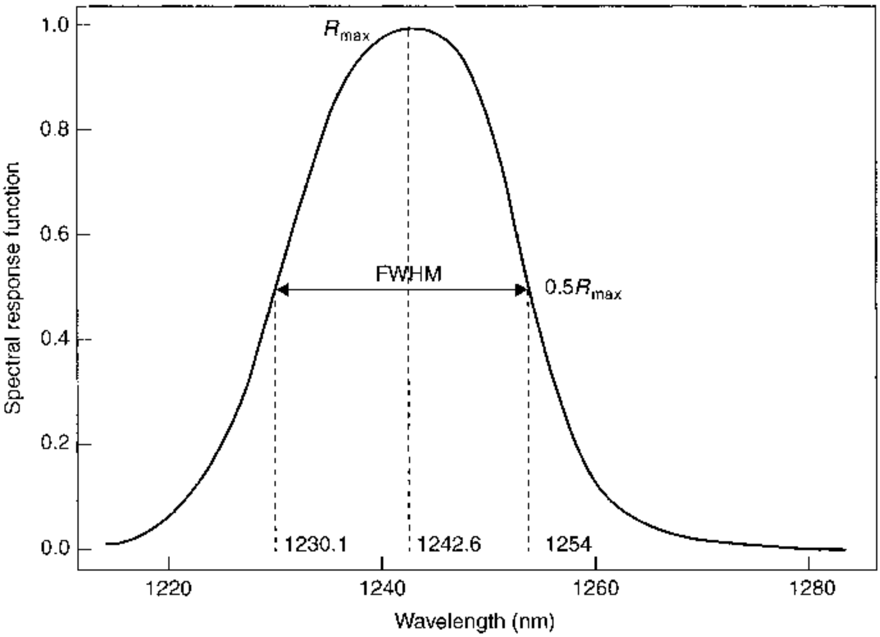

Figure 1.9 Central wavelength and FWHM of the sensor spectral response function using a simple traditional method.

width at half maximum (FWHM), which is shown in Fig. 1.9. This is the sensor response function of MODIS band 5. The central wavelength of a spectral band responds to the maximum value of the response function. This approach is very empirical and simple, but may not be appropriate if the response function is not skew and irregular.

Palmer (1984) suggested the moment method for determining the central wavelength λ_c and effective bandwidth $\Delta\lambda$. The pertinent equations are

$$\lambda_c = \frac{\int_{\lambda_{min}}^{\lambda_{max}} f(\lambda)\,\lambda\,d\lambda}{\int_{\lambda_{min}}^{\lambda_{max}} f(\lambda)\,d\lambda} \tag{1.17}$$

$$\sigma^2 = \frac{\int_{\lambda_{min}}^{\lambda_{max}} f(\lambda)\,\lambda^2\,d\lambda}{\int_{\lambda_{min}}^{\lambda_{max}} f(\lambda)\,d\lambda} - \lambda_c^2 \tag{1.18}$$

$$\lambda_1 = \lambda_c - \sqrt{3}\,\sigma \tag{1.19}$$

$$\lambda_2 = \lambda_c + \sqrt{3}\,\sigma \tag{1.20}$$

$$\Delta\lambda = \lambda_2 - \lambda_1 = 2\sqrt{3}\,\sigma \tag{1.21}$$

where $\lambda_{\min}$ and $\lambda_{\max}$ are the minimum and maximum wavelengths of the waveband beyond which the sensor spectral response function is zero. The spectral response functions of ETM + and MODIS visible and near-IR (VNIS) sensors are displayed in Fig. 1.8. The digital files of these two sensors as well as others are included in the CD-ROM for ease of reference. For MODIS band 5, the calculated central wavelength is 1242.1 nm with $\lambda_1 =$ 1226.47 nm and $\lambda_2 = 1257.79$ nm, and the effective bandwidth is 31.3 nm. If we use the simple method as illustrated in Fig. 1.9, FWHM = 23.9 nm. The difference is significant.

The number of multispectral bands varies dramatically from one sensor to another. Figure 1.10 illustrates the spectral bands and their spectral ranges of some common spaceborne multispectral sensors in the visible and near-IR spectrum for land applications. Hyperspectral sensors are discussed in Section 8.1.2.

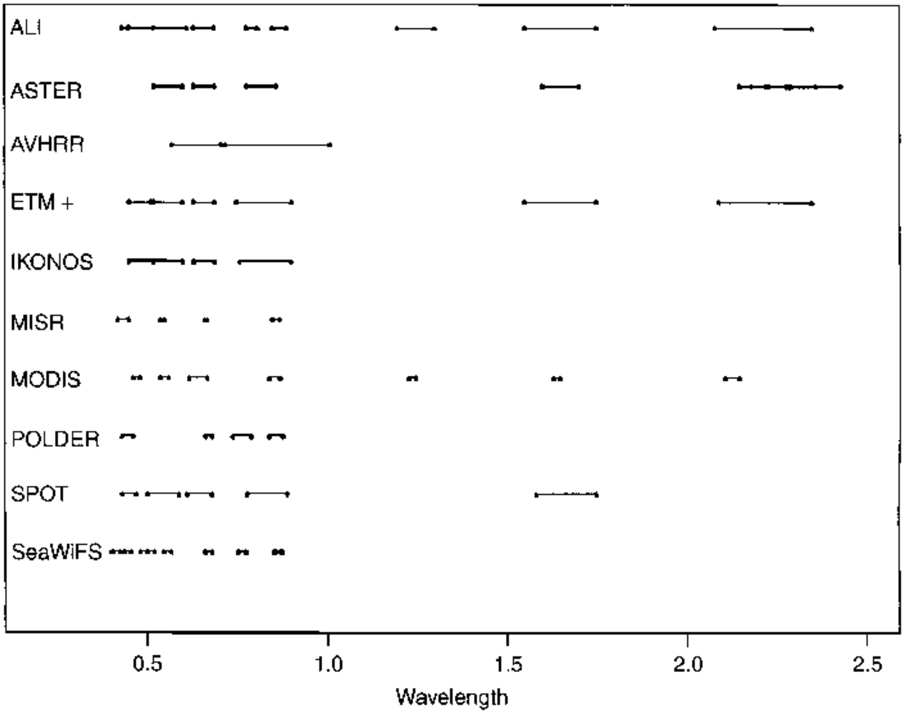

Figure 1.10 Illustration of multispectral bands and their spectral ranges of some typical land sensors.

In Fig. 1.10, SPOT bands actually represent SPOT VEGTATION. SPOT1, -2, and -3 HRV has three multispectral bands: green, red, and near IR. SPOT4 and -5 HRV has one extra band in middle IR. Those bands have almost identical spectral coverage with the VEGETATION bands.

1.3.5.2 Spatial Response

The spatial response of the sensor is often characterized by a parameter called *modulation transfer function* (MTF), a precise measurement of details and contrast made in the frequency domain. Each component of the sensor imaging system has a characteristic frequency response. The beauty of working in the frequency domain is that the response of the entire system (or group of components) can be calculated by multiplying the responses of each component. The Fourier transform of the MTF, which is fast and easy to perform on modern computers using the fast Fourier transform (FFT) algorithm, is called *point spread function* (PSF) in the spatial domain. In fact, the Fourier transform of PSF is called the *optical transfer function* (OTF), and the normalized magnitude of the OTF is MTF. The sensor spatial response function is often modeled as a Gaussian PSF:

$$h(x,y)=\frac{1}{2\pi\sigma^2}\exp\left(-\frac{x^2+y^2}{2\sigma^2}\right) \tag{1.22}$$

where σ is one-half the number of scene cells (on a side) in the sensor ground instantaneous field of view (IFOV). If we can assume that PSF is a separable function with respect to the (x, y) coordinate system, then $\mathrm{PSF}(x,y)=\mathrm{LSF}_x(x)\cdot\mathrm{LSF}_y(y)$ where PSF and LSF are denoted as point spread and linespread functions.

There are many different techniques for estimating the MTF of a sensor system in a laboratory, such as the impulse input method, sinusoidal input method, knife-edge input method, and pulse input method. However, only some of them can be used for estimating the sensor MTF from remote sensing imagery. For example, the pulse input method was used to measure Landsat TM MTF in which the source for the pulse is the bridge over the San Francisco Bay (Schowengerdtet al. 1985). Both the pulse and edge methods were used to estimate IKONOS sensor MTF (Helder and Choi 2001). Ruiz and Lopez (2002) derived the normalized PSF matrix of the SPOT imagery using the edge method, which is listed in Table 1.4. The TM PSF is shown in Fig. 1.11.

From MTF we can define the effective instantaneous field of view (EIFOV), which is the spatial dimension equivalent to half a cycle of the spatial frequency where the MTF falls to 0.5 (NASA 1973). The measured PSF of the overall TM system is shown in Fig. 1.10. It is not an ideal square shape with a width of 30 m, which implies that signals beyond the 30 × 30-m grid also contribute to the current pixel value. In other words, the current pixel value depends on the values of its neighboring pixels. In fact, the

TABLE 1.4 SPOT Sensor Point Spread Function (PSF) Matrix

0.0017	0.0018	0.0020	0.0022	0.0024	0.0022	0.0020	0.0018	0.0017
0.0018	0.0050	0.0057	0.0064	0.0071	0.0064	0.0057	0.0050	0.0018
0.0020	0.0057	0.0167	0.0201	0.0236	0.0201	0.0167	0.0057	0.0020
0.0022	0.0064	0.0201	0.0317	0.0448	0.0317	0.0201	0.0064	0.0022
0.0024	0.0071	0.0236	0.0448	0.6513	0.0448	0.0236	0.0071	0.0024
0.0022	0.0064	0.0201	0.0317	0.0448	0.0317	0.0201	0.0064	0.0022
0.0020	0.0057	0.0167	0.0201	0.0236	0.0201	0.0167	0.0057	0.0020
0.0018	0.0050	0.0057	0.0064	0.0071	0.0064	0.0057	0.0050	0.0018
0.0017	0.0018	0.0020	0.0022	0.0024	0.0022	0.0020	0.0018	0.0017

Source: Ruiz and Lopez (2002).

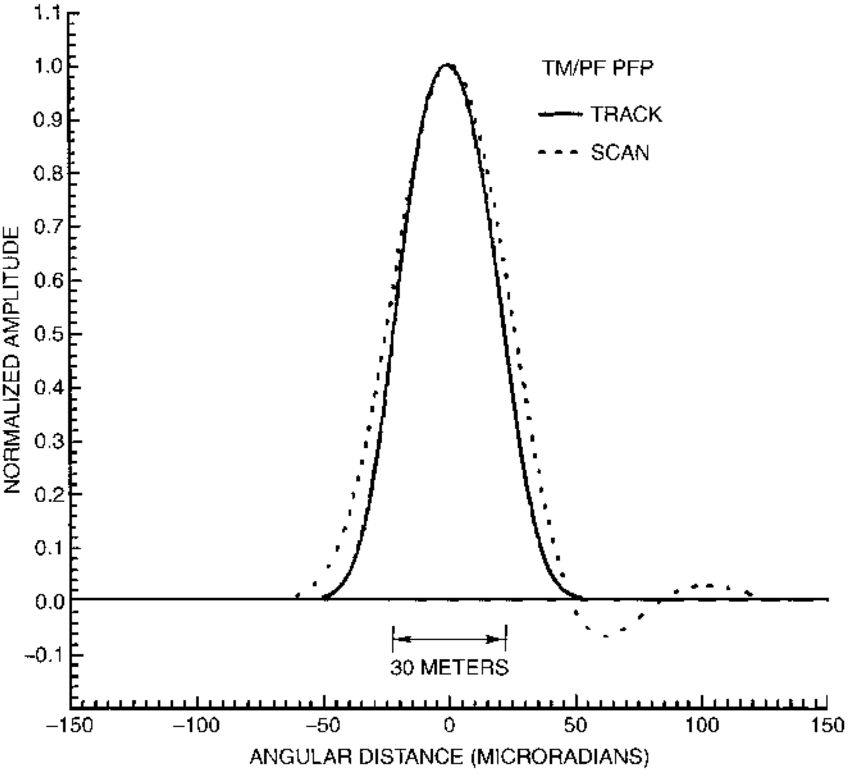

Figure 1.11 TM PSF function at both track and scan directions. [From Markham (1985), *IEEE Trans. Geosci. Remote Sens*. Copyright © 1985 with permission from IEEE.]

TABLE 1.5 Spatial Resolution (in meters) of Some Typical Multispectral Remote Sensors

	Spectral Bands	
Sensors	Multispectral	Panchromatic
ALI	All bands: 30	10
ASTER	Bands 1–3: 15 Bands 4–9: 30	
AVHRR	All bands: 1000	
ETM +	Bands 1–5 and 7: 30 Band 6: 60	15
GLI	Bands 1–6: 250	
IKONOS	4	1
MERIS	300	
MISR	1000	
MODIS	Bands 1–2: 250 Bands 3–7: 500 Other bands: 1000	
POLDER	6000 × 8000	
SPOT 1–4	All bands: 20	10
SPOT-5	Bands 1–3: 10 Band 4: 20	5/2.5
SPOT-VEGETATION	All bands: 1000	
SeaWiFS	All bands: 1100	

EIFOVs for TM 1–4 are 35.9 and 32.1 m for TM bands 1–4 in the scan and track directions, respectively. For bands 5 and 7, the EIFOVs are 35.7 and 33.3 m in the scan and track directions, respectively (Markham 1985).

The impacts of sensor PSF on land cover classifications are evaluated by Townshend et al. (2000) and Huang et al. (2002).

For ease of reference, Table 1.5 lists the spatial resolutions of some typical land sensors. Note that the spatial resolution of some off-nadir viewing sensors is the same as that at nadir. The acronyms of these sensors are listed in the Frontmatter of the book.

1.3.6 Mapping and Binning

After navigation of the sensor output, the geolocation of the central point and other parameters of each measurement need to be determined. Since each measurement corresponds to a surface region with different shapes and sizes, an important process in the image generation is to bin these measurements into a regular two-dimensional array with one particular map projection.

Selection of a map projection becomes very important when we are concerned with the global monitoring because any map projection that

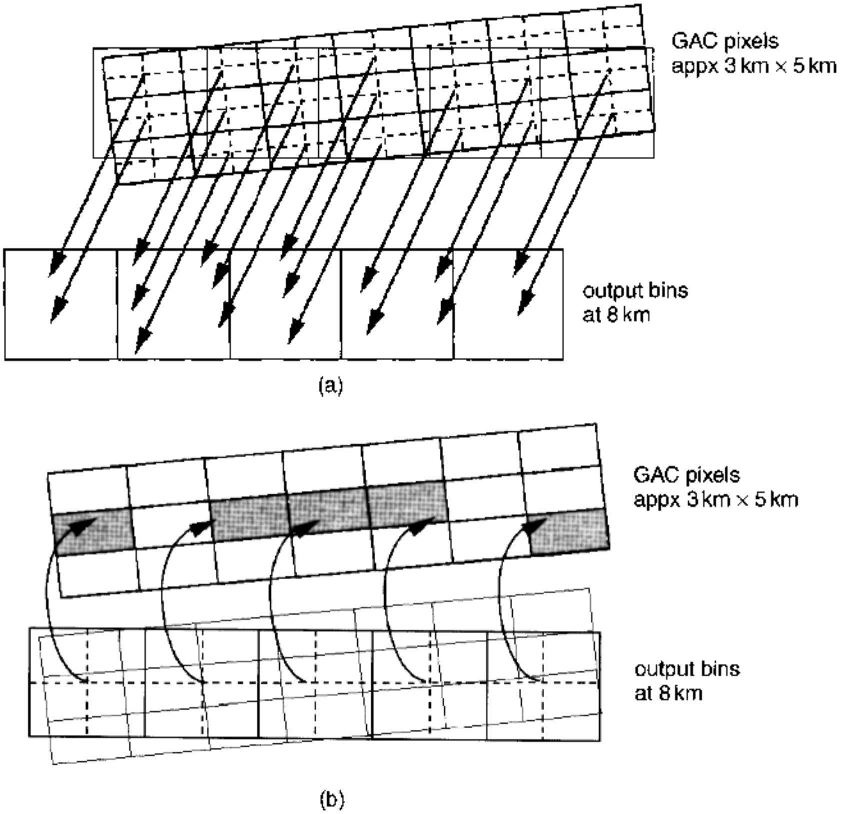

Figure 1.12 Illustration of both forward (a) binning and inverse (b) binning methods. [From James and Kalluri (1994), *Int. J. Remote Sens.* Reproduced by permission of Taylor & Francis, Ltd.]

transforms the curve surface to a flat plane introduces errors. Many equal-area map projections have been proposed and used in the remote sensing product generation, such as the space oblique mercator or the Universal Transverse Mercator (UTM) projection for TM/ETM + imagery (Snyder 1981), the interrupted Goode homolosine projection for AVHRR (Steinwand 1994), the intergerized sinusoidal projection and Lambert azimuthal projection for MODIS (Masuoka et al. 1998), and space oblique mercator projection for MISR (Diner et al. 1998).

There are two general methods for mapping each measurement to the output bins: *forward binning*, where the location of each measurement is used to locate the output bin; and *inverse binning*, where the location of the output bin is used to locate each measurement to the bin. Figure 1.12 illustrates the two binning methods for generating AVHRR Pathfinder Land data from the Global Area Coverage (GAC) data (James and Kalluri 1994).

No matter which binning method is used, the original observations have to be resampled. There are several resampling methods used in remote sensing, including nearest-neighbor, bilinear interpolation, and cubic convolution (e.g., Schowengerdt 1997). When ordering Landsat ETM + imagery from USGS EDC, the user can specify a specific resampling method.

1.4 SUMMARY

This is an introductory chapter that lays the foundation for the rest of the book. It discusses various radiometric variables and then describes the major components of a remote sensing modeling system. Most of the discussion was very brief, but landscape generation, spectral and spatial sensor characteristics, and mapping and binning were discussed in a bit more detail. Because of the scope of this book, readers should consult the references cited in the text for further details on some components such as navigation modeling and image mapping and binning.

REFERENCES

Anderson, G. P., Berk, A., Acharya, P. K., Matthew, M. W., Bernstein, L. S., Chetwynd, J. H., Dothe, H., Adler-Golden, S. M., Ratkowski, A. J., Felde, G. W., Gardner, J. A., Hoke, M. L., Richtsmeier, S. C., and Jeong, L. S. (2001), MODTRAN4, version 2: Radiative transfer modeling, *Proc. SPIE*, 455–459.

Chellappa, R. (1985), Two-dimensional discrete gaussian markov random field models for image processing, in *Progress in Pattern Recognition*, L. N. Kanal and A. Rosenfeld, eds., Elsevier Science Publishers, pp. 79–112.

Cressie, N. (1993), *Statistics for Spatial Data*, rev. ed., Wiley.

Cross, G. R. and Jain, A. K. (1983), Markov random field texture models, *IEEE Trans. Pattern Anal. Mach. Intel.* **5**: 25–39.

Deutsch, C. V. and Journel, A. G. (1992), *GSLIB: Geostatistical Software Library and User's Guide*, Oxford Univ. Press.

Diner, D., Beckert, J. C., Reilly, T. H., Bruegge, C. J., Conel, J. E., Kahn, R. A., Martonchik, J. V., et al. (1998), Multi-angle imaging spectroradiometer (MISR) instrument descrition and experiment overview, *IEEE Trans. Geosci. Remote Sens.* **36**: 1072–1097.

Dubes, R. C. and Jain, A. K. (1989), Random field models in image analysis, *J. Appl. Stat.* **16**: 131–164.

Emery, W. J., Brown, J., and Nowak, Z. P. (1989), AVHRR image navigation: Summary and review. *Photogram. Eng. Remote Sens.* **55**: 1175–1183.

Fisher, Y., ed. (1995), *Fractal Image Compression: Theory and Application to Digital Images*, Springer-Verlag.

Gao, B. C. and Green, R. O. (1995), Presence of terrestrial atmospheric gas absorption bands in standard extraterrestrial solar irradiance curves in the near-infrared spectral region, *Appl. Opti.* **34**: 6263–6268.

Hartmann, D. L., Bretherrton, C. S., Charlock, T. P., Chou, M. D., Del Genio, A., Dickinson, R. E., Fu, R., Houze, R. A., King, M. D., Lau, K. M., Leovy, C. B., Sorooshian, S., Washburne, J., Wielicki, B., and Willson, R. C. (1999), Radiation, clouds, water vapor, precipitation, and atmospheric circulation, in *EOS Science Plan*, NASA GSFC, pp. 39–114.

Helder, D. and Choi, J. (2001), MTF modeling and error analysis for high spatial resolution satellite sensors.

Huang, C., Townshend, J. R. G., Liang, S., Kalluri, S. N. V., and DeFries, R. S. (2002), Impact of sensor's point spread function on land cover characterization: Assessment and deconvolution, *Remote Sens. Environ.* **80**: 203–212.

Isaaks, E. and Srivastava, R. M. (1989), *An Introduction to Applied Geostatistics*, Oxford Univ. Press.

James, M. E. and Kalluri, S. N. V. (1994), The pathfinder AVHRR land data set: An improved coarse resolution data set for terrestrial monitoring, *Int. J. Remote Sens.* **15**: 3347–3363.

Jeng, F. C., Woods, J. W. and Rastogi, S. (1993), Compound Gauss-Markov random fields for parallel image processing, in *Markov Random Fields: Theory and Application*, R. Chellappa and A. K. Jain, eds., Academic Press, pp. 11–38.

Journel, A. G. and Huijbregts, C. J. (1978), *Mining Geostatistics*, Academic Press.

Kerekes, J. P., and Landgrebe, D. A. (1991), An analytical model of Earth-observational remote sensing systems, *IEEE Trans. Geosci. Remote Sens.* **21**: 125–133.

Liang, S. and Strahler, A. eds. (2000), Land surface bidirectional reflectance distribution function (BRDF): Recent advances and future prospects, *Remote Sens Rev* **18**: 83–551.

Mandelbrot, B. (1983), *The Fractal Geometry of Nature*, Freeman.

Markham, B. L. (1985), The Landsat sensors' spatial responses, *IEEE Trans. Geosci. Remote Sens.* **23**: 864–875.

Martonchik, J. V., Bruegge, C. J., and Strahler, A. H. (2000), A review of reflectance nomenclature used in remote sensing, *Remote Sensing Rev.* **19**: 9–20.

Masuoka, E., Fleig, A., Wolfe, R., and Patt, F. (1998), Key characteristics of MODIS data products. *IEEE Trans. Geosci. Remote Sens.* **36**: 1313–1323.

Milman, A. S. (1999), *Mathematical Principles of Remote Sensing: Making Inferences from Noisy Data*, Sleeping Bear Press.

NASA (1973), Advanced scanners and imaging systems for earth observations, *NASA Tech. Report* SP-335.

Palmer, J. M. (1984), Effective bandwidths for Landsat-4 and Landsat-d' multispectral scanner and thematic mapper subsystems, *IEEE Trans. Geosci. Remote Sens.* **22**: 336–338.

Prusinkiewicz, P. and Lindenmayer, A. (1990), *The Algorithmic Beauty of Plants*, Springer-Verlag.

Ruiz, C. P. and Lopez, F. J. A. (2002), Restoring SPOT images using PSF-derived deconvolution filters, *Int. J. Remote Sens.* **23**: 2379–2391.

Schott, J. R. (1997), *Remote Sensing: The Image Chain Approach*, Oxford Univ. Press.

Schowengerdt, R., Archwamety, C., and Wrigley, R. C. (1985), Landsat Thematic Mapper image derived mtf, *Photogram. Eng. Remote Sens.* **51**: 1395–1406.

Schowengerdt, R. A. (1997), *Remote Sensing, Models and Methods for Image Processing*, 2nd ed., Academic Press.

Snyder, J. P. (1981), Space oblique mercator projection—mathematical development, *U.S. Geol. Survey Bull.* 1518.

Steinwand, D. R. (1994), Mapping raster imagery to the interrupted good homolosine projection, *Int. J. Remote Sens.* **15**: 3463–3471.

Strahler, A. H., Woodcock, C. E., and Smith, J. A. (1986), On the nature of models in remote sensing, *Remote Sens. Envir.* **20**: 121–139.

Townshend, J. G. R., Huang, C., Kalluri, S., DeFries, D., Liang, S., and Yang, K. (2000), Beware of per-pixel characterization of land cover, *Int. J. Remote Sens.* **21**: 839–843.